Review:

A look at field manipulation and antenna design using 3D transformation electromagnetics and 2D surface electromagnetics[*]

Peng-fei ZHANG[‡1], Yu-kai YAN[1], Ying LIU[1], Raj MITTRA[2,3]

[1]School of Electrical Engineering, Xidian University, Xi'an 710071, China

[2]Department of Electrical Engineering and Computer Science, University of Central Florida, Orlando, FL 32816, USA

[3]Department of Electrical and Computer Engineering, King Abdulaziz University, Jeddah 22254, Saudi Arabia

E-mail: zhangpf@mail.xidian.edu.cn; yyk@stu.xidian.edu.cn; liuying@mail.xidian.edu.cn; rajmittra@ieee.org

Abstract: While many techniques have been developed for the design of different types of antennas, such as wire antenna, patch antenna, lenses, and reflectors, these cannot be said general-purpose strategies for the synthesis and design of antennas to achieve the performance characteristics specified by users. Recently, there has been an increasing need for the development of antenna design techniques because of the advent of 5G and a variety of space, defense, biological, and similar applications, for which a robust and general-purpose design tool is not to be developed. The main objective of this study is to take a look at antenna design from the field manipulation point of view, which has the potential to partially fulfill this need. We review the existing field manipulation techniques, including field transformation methods based on Maxwell's and wave equations, point out some limitations of these techniques, and then present ways to improve the performance of these methods. Next, we introduce an alternative approach for field manipulation based on two-dimensional (2D) metasurfaces, and present laws of the generalized reflection and refraction that are based on 2D surface electromagnetics. Then, we explore how to overcome the limitations of conventional reflection and refraction processes that are strictly bounded by the critical angle. Finally, we provide some application examples of field manipulation methods in the antenna design, with a view on developing a general-purpose strategy for antenna design for future communication.

1 Introduction

Design of antennas for many applications, such as wireless communication, radar detection, radio astronomy, wireless power transmission, and cloaking, is based on manipulations of current distributions and electromagnetic fields. There has been no available systematic approach to manipulating the fields before the introduction of the method of transformation optics (TO) (Leonhardt, 2006; Pendry et al., 2006), also known as transformation electromagnetics (TEM) and surface electromagnetics (SEM) (Yang F and Rahmat-Samii, 2019), which has attracted considerable attention.

TO provides an elegant theoretical approach for the electromagnetic field manipulation method by relating the electromagnetic fields in one coordinate system to another (Pendry et al., 2006). Some examples of TO-based design, including cloaks designed to conceal a target, are shown in Figs. 1a–1c. These cloaks can be used to shield an antenna from the fields scattered by a mounting platform or from other antennas operating in close proximity to meet the electromagnetic compatibility (EMC) requirements, as shown in Fig. 1d (Kwon and Werner, 2008).

In contrast to TO, SEM provides a method to manipulate the reflection and refraction of electromagnetic waves by a surface to overcome some of the problems encountered by TO, such as finding the materials needed by the TO paradigm to affect the field transformation from one coordinate to another. Fig. 1e shows the typical SEM-based design, i.e., a space-time-coding digital metasurface that can transform an impinging single frequency beam into a group of desired beams at different frequencies. Such a surface has been used as an antenna in an advanced imaging system (Li et al., 2019). However, the SEM method has problems, especially when attempting to manipulate both the magnitudes and phases of the fields.

In this study, we introduce an alternative way to look at TO and SEM approaches in the antenna design, and focus on the boundary and interface aspects of field manipulation using three-dimensional (3D) transformation electromagnetics and two-dimensional (2D) surface electromagnetics.

We review the TO, which is based on the coordinate transformation of Maxwell's equations (Pendry et al., 2006), and discuss the issues of uniqueness of transformation and impedance matching for a given geometry mapping. Then, we review the concept of wave-equation-based (WEB) transformation which, in contrast to anisotropic ε and μ required in the implementation of the TO algorithm, works only with isotropic dielectric materials. Advantages and limitations of WEB transformation are discussed.

Next, we turn to another attractive approach to manipulating the field, namely SEM, which circumvents the need for anisotropic and inhomogeneous dielectric and magnetic materials by the TO paradigm. We first introduce the concepts of generalized reflection and refraction based on the 2D surface electromagnetics approach, and then explore ways to overcome the limitations of conventional reflection and refraction processes set by the critical angle.

Illustrative examples of applications of field manipulation methods to antenna design are presented. The topic of performing a mathematical operation by field manipulation to design complex antenna systems is discussed.

Finally, we make brief conclusions and mention some areas of field manipulation in antenna design for further exploration.
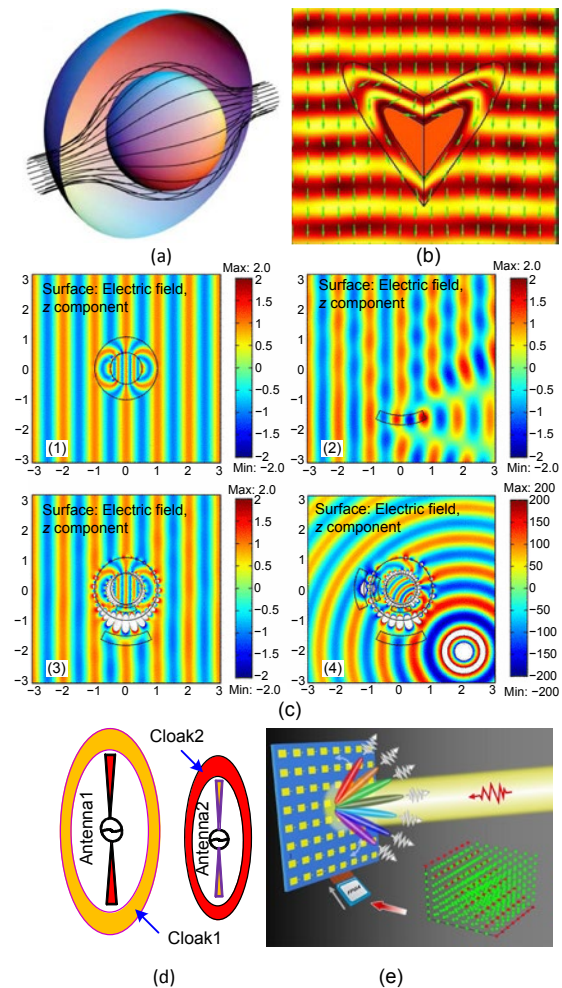

Fig. 1 Classical cloak (a), cloaks for arbitrarily shaped objects (b), cloak that can cloak objects at a distance outside the cloaking shell (c), cloaking antenna for electromagnetic compatibility (d), and antenna using space-time-coding digital metasurfaces (e)

(a) is reprinted from Schurig et al. (2006), Copyright 2006, with permission from OSA, licensed under CC BY 4.0. (b) is reprinted from Jiang et al. (2008), Copyright 2008, with permission from APS, licensed under CC BY 4.0. (c) is reprinted from Lai et al. (2009), Copyright 2009, with permission from APS, licensed under CC BY 4.0. (e) is reprinted from Zhang L et al. (2018), Copyright 2018, with permission from Springer Nature, licensed under CC BY 4.0

2 Transformation optics and its generalization

In this section, we briefly describe the TO-based approach to field manipulation. The classical TO paradigm accomplishes field mapping using the coordinate transformation of Maxwell's equations from

unprimed to primed coordinates through a one-to-one mapping relationship, as illustrated in Fig. 2 (Pendry et al., 2006). Mathematically speaking, a suitable choice of mapping such as $r'=[(b-a)/b]r+a$ can map the mesh within the circular region in the original free space in Fig. 2a to that of the annular region in Fig. 2b. The question is how to ensure that the electromagnetic (EM) field within the circular free-space region in Fig. 1c can be identically mapped to the annular region in Fig. 1d, which consequently makes the electromagnetic waves traverse the region bypassing the inner blank region, thereby cloaking the obstacle located in this region.

Assuming that the Cartesian coordinates (original space) in Fig. 2a are (x, y, z) and that the coordinates of the mapped space in Fig. 2b are (x', y', z'), one can set up a one-to-one mathematical mapping relationship between Figs. 2a and 2b. The Jacobian matrices of a mapping can be expressed as

$$\Lambda = \begin{bmatrix} \dfrac{\partial x'}{\partial x} & \dfrac{\partial x'}{\partial y} & \dfrac{\partial x'}{\partial z} \\ \dfrac{\partial y'}{\partial x} & \dfrac{\partial y'}{\partial y} & \dfrac{\partial y'}{\partial z} \\ \dfrac{\partial z'}{\partial x} & \dfrac{\partial z'}{\partial y} & \dfrac{\partial z'}{\partial z} \end{bmatrix}, \Lambda^{-1} = \begin{bmatrix} \dfrac{\partial x}{\partial x'} & \dfrac{\partial x}{\partial y'} & \dfrac{\partial x}{\partial z'} \\ \dfrac{\partial y}{\partial x'} & \dfrac{\partial y}{\partial y'} & \dfrac{\partial y}{\partial z'} \\ \dfrac{\partial z}{\partial x'} & \dfrac{\partial z}{\partial y'} & \dfrac{\partial z}{\partial z'} \end{bmatrix}. \quad (1)$$
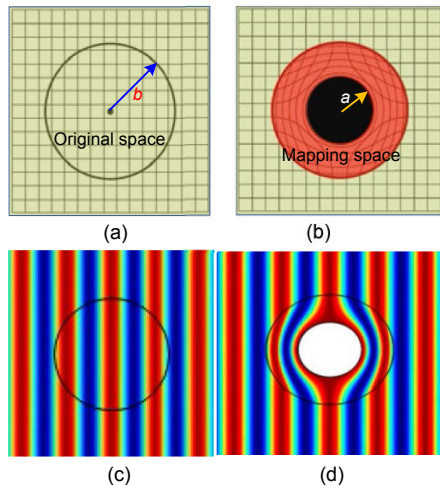

Fig. 2 Schematic of stealth cloak: (a) original space; (b) mapping space; (c) field of the original space; (d) field of the mapping space

Additionally, if the source and medium of the original and mapping spaces satisfy the relationships below:

$$\begin{cases} [\varepsilon'] = \Lambda[\varepsilon]\Lambda^{\mathrm{T}}/|\det \Lambda|, \\ [\mu'] = \Lambda[\mu]\Lambda^{\mathrm{T}}/|\det \Lambda|, \\ J' = \Lambda J/|\det \Lambda|, \\ \rho' = \rho/|\det \Lambda|, \end{cases} \quad (2)$$

where ρ and J are the charge and current density, respectively, and ε and μ are the permittivity and permeability of the medium, respectively (The quantity of the mapping space is marked by adding a prime, to distinguish it from the quantity of the original space), then the fields in these two spaces satisfy identical Maxwell's equations in their own coordinate systems, expressed as

$$\begin{cases} \nabla H = \dfrac{\partial \varepsilon E}{\partial t} + J, \\ \nabla E = -\dfrac{\partial \mu H}{\partial t}, \\ \nabla D = \rho, \\ \nabla B = 0, \end{cases} \begin{cases} \nabla' H' = \dfrac{\partial \varepsilon' E'}{\partial t} + J', \\ \nabla' E' = -\dfrac{\partial \mu' H'}{\partial t}, \\ \nabla' D' = \rho', \\ \nabla' B' = 0, \end{cases} \quad (3)$$

where E and D are the electric field intensity and electric displacement vector respectively, and H and B are the magnetic field intensity and induction intensity, respectively.

The corresponding electromagnetic field solutions to Eq. (3) satisfy the one-to-one mapping relationship, expressed as

$$\begin{cases} E' = (\Lambda^{-1})^{\mathrm{T}} E, & D' = \Lambda D/|\det \Lambda|, \\ H' = (\Lambda^{-1})^{\mathrm{T}} H, & B' = \Lambda B/|\det \Lambda|. \end{cases} \quad (4)$$

Hence, as shown in Fig. 2, if we choose the materials in these regions in accordance with Eq. (2), the EM field within the circular free-space region in Fig. 1c can be identically mapped to the annular region in Fig. 1d as desired, which consequently generates a cloak for the obstacle located in the region of $r'<a$.

Note that the transformation is implemented only between the regions within the circular region in Fig. 1c and within the annular boundary between $a<r'<b$ in Fig. 2d, while the region outside remains unaffected by the transformation. It is necessary to ensure that the wave can propagate through the interface ($r=b$) between the transformed and

untransformed regions. To achieve this goal, it is necessary to ensure that the transformed mesh near the interface tends to become identical to that in the original space, to guarantee that the impedance near the interface has a smooth transition, expressed as

$$\eta' = \sqrt{\mu'/\varepsilon'} \rightarrow \sqrt{\mu_0/\varepsilon_0} = \eta_0, \qquad (5)$$

where η is the impedance.

However, the implementation of this condition often poses practical difficulties, the difficulty of which is to find the realizable materials for the cloak with the desired properties.

For another typical application of TO to antenna design, i.e., the design of a flat lens based on TO (Fig. 3), the problem becomes even more obvious.

For this geometry, the convex region is mapped to a rectangular one. However, the required high compression ratio of the mesh in the central region requires the use of a material with high permittivity in the center region. This, in turn, introduces mismatch on the interface between the lens and free space, unless we transform a much larger region that includes both the lens and the medium surrounding it, which sacrifices the compactness of the design.

A more general transformation is presented as (Zhang PE et al., 2019)

$$\begin{cases} [\varepsilon''] = \dfrac{\zeta}{\xi} \varLambda[\varepsilon]\varLambda^{\mathrm{T}} / |\det \varLambda|, \\[2mm] [\mu''] = \dfrac{\xi}{\zeta} \varLambda[\mu]\varLambda^{\mathrm{T}} / |\det \varLambda|, \\[2mm] \boldsymbol{J}'' = \dfrac{1}{\xi} \varLambda \boldsymbol{J} / |\det \varLambda|, \\[2mm] \rho'' = \dfrac{1}{\xi} \rho / |\det \varLambda|, \end{cases} \begin{cases} \boldsymbol{E}'' = \dfrac{1}{\zeta} (\varLambda^{-1})^{\mathrm{T}} \boldsymbol{E}, \\[2mm] \boldsymbol{H}'' = \dfrac{1}{\xi} (\varLambda^{-1})^{\mathrm{T}} \boldsymbol{H}, \\[2mm] \boldsymbol{D}'' = \dfrac{1}{\xi} \varLambda \boldsymbol{D} / |\det \varLambda|, \\[2mm] \boldsymbol{B}'' = \dfrac{1}{\zeta} \varLambda \boldsymbol{B} / |\det \varLambda|, \end{cases} \quad (6)$$

where ξ and ζ are the independent coefficients that can be freely selected.

Eq. (6) represents alternate mapping relationships that are different from those in Eq. (2) (Pendry et al., 2006), and the related characteristic impedance now becomes

$$\eta'' = \sqrt{\frac{\mu''}{\varepsilon''}} = \frac{\xi}{\zeta}\eta' = \frac{\xi}{\zeta}\sqrt{\frac{\mu'}{\varepsilon'}} \rightarrow \frac{\xi}{\zeta}\sqrt{\frac{\mu_0}{\varepsilon_0}} = \frac{\xi}{\zeta}\eta_0. \quad (7)$$
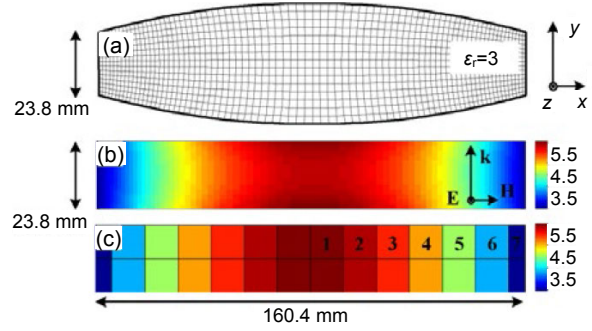

Fig. 3   **Convex and flat lens based on coordinate transformation: (a) convex lens with nearly orthogonal mapping; (b) flat lens with the permittivity map consisting of 80×15 blocks; (c) flat lens with the permittivity map consisting of 14×2 blocks**
Reprinted from Yang R et al. (2011), Copyright 2011, with permission from IEEE

This impedance is no longer the same as the characteristic impedance of the original space on the transformation boundary, even though these two regions share a common boundary and the mesh grid on the interface. Moreover, since ζ and ξ are two independent coefficients, any desired characteristic impedance can be obtained by choosing ζ and ξ, meaning that the transmitted system can be embedded in a space with impedance of $\xi\eta_0/\zeta$ without introducing serious reflections on the interface.

With an appropriate choice of ζ and ξ, we can modify the impedance of materials located at the central region of the flat lens, to avoid mismatch on the interface between the lens and the free space. This strategy can be used to design a cloak that can be embedded in the medium with any given impedance.

Remind that Eqs. (2) and (6) need non-uniform anisotropic material, which is hard to realize even when metamaterials are employed (Mittra et al., 2016).

3   Wave-equation-based method of transformation

To mitigate the issue of realizing 3D materials required by the TO-based transformation of Maxwell's equations, a 2D version of the transformation equation has been derived (Liu R et al., 2009). This method has the advantage that only isotropic dielectric is required; however, its application is

limited by the following four assumptions (Zhang PF et al., 2019):

1. The original and mapping spaces are passive. The electric field contains only one component, i.e., $E = \hat{z}E_z$. The related wave equation is expressed as

$$\nabla^2 E_z + w^2 \mu_0 \varepsilon E_z = 0, \qquad (8)$$

where w is the angular frequency.

2. The permeability of the original and mapping spaces is μ_0.

3. The mapping relationship determined by $x'(x, y)$ and $y'(x, y)$ is a conformal mapping. Hence, in the complex plane, it can be expressed as $\omega'(x', y') = \omega'(\omega) = x'(x, y) + jy'(x, y)$, where $\omega = x + jy$. x, y, x', and y' satisfy the Cauchy-Riemann condition, expressed as

$$\frac{\partial x'}{\partial x} = \frac{\partial y'}{\partial y}, \quad \frac{\partial y'}{\partial x} = -\frac{\partial x'}{\partial y}. \qquad (9)$$

4. The transformation is 2D, implying that both the field and the medium extend to infinity uniformly in the z direction.

Now, we discuss the permittivity-only design. Expanding the Hamiltonian operator ∇ in Eq. (8) by the differential relationships of $\frac{\partial}{\partial x} = \frac{\partial}{\partial x'}\frac{\partial x'}{\partial x} + \frac{\partial}{\partial y'}\frac{\partial y'}{\partial x}$ and $\frac{\partial}{\partial y} = \frac{\partial}{\partial x'}\frac{\partial x'}{\partial y} + \frac{\partial}{\partial y'}\frac{\partial y'}{\partial y}$ and the Cauchy-Riemann condition, the wave equation in the coordinate system (x', y') can be written as

$$\nabla'^2 E_z' + w^2 \mu_0 \varepsilon E_z' \left| \frac{\mathrm{d}\omega'}{\mathrm{d}\omega} \right|^{-2} = 0, \qquad (10)$$

where

$$\begin{cases} \frac{\mathrm{d}\omega'}{\mathrm{d}\omega} = \frac{\partial x'}{\partial x} + j\frac{\partial y'}{\partial x} = \frac{\partial y'}{\partial y} - j\frac{\partial x'}{\partial y}, \\ \left| \frac{\mathrm{d}\omega'}{\mathrm{d}\omega} \right|^2 = \left(\frac{\partial x'}{\partial x} \right)^2 + \left(\frac{\partial y'}{\partial x} \right)^2 = \left(\frac{\partial y'}{\partial y} \right)^2 + \left(\frac{\partial x'}{\partial y} \right)^2. \end{cases} \qquad (11)$$

Therefore, if the mapping space is filled with a material satisfying

$$\varepsilon'(x', y') = \varepsilon(x, y) \left| \frac{\mathrm{d}\omega'}{\mathrm{d}\omega} \right|^{-2}, \qquad (12)$$

then the field in this space will satisfy the wave equation, expressed as follows:

$$\nabla'^2 E_z' + w^2 \mu_0 \varepsilon' E_z' = 0. \qquad (13)$$

It can be seen that the electric field components of the original and mapping spaces satisfy the same equation and their solution can be mapped to each other, expressed as

$$E_z'(x', y') = E_z(x, y). \qquad (14)$$

Since this method is based on the wave equation, it is referred to as the WEB transformation. We can use it to design a 2D carpet cloak by combining Eq. (12) with a method similar to the transform method in Fig. 2. Note that Eq. (12) requires isotropic permittivity values that are more easily realized than those required by TO.

4 Field manipulation based on 2D surface electromagnetics

Even though the method based on transformation is elegant in theory, its use has been limited because the anisotropic material needed to form the cloak is difficult to realize, especially for practical applications to realistic targets, such as an airplane or a missile. Hence, a natural way to mitigate this problem is to develop a method which can manipulate the field during reflection or refraction by a 2D surface. There are many publications on this topic. Yu et al. (2011, 2013) had led to research based on the surface electromagnetics, also referred to as generalized Snell's law (GSL) and the gradient optical method. In contrast to the TO approach, the surface approach is designed to control the reflection or refraction of the EM waves when they travel through an ultrathin surface. This is accomplished by working with a non-uniform surface (Yu et al., 2011) and gradually manipulating magnitude, phase, and polarization (Yang F and Rahmat-Samii, 2019), or even time-domain modulation (Zhang L et al., 2018) of the electromagnetic wave, as it propagates through the surface.

In this section, we introduce the GSL from the point of view of phase matching. It not only presents a

clear explanation of the principle upon which the manipulation of the reflection or refraction by phase shift is based, but also guides us to strategic ways by which we can overcome the limitations of the critical angle based on traditional Snell's law. Some examples of the field manipulation of electromagnetic waves or fields are introduced in this section to demonstrate its capability.

4.1 Generalized Snell's law

It is well known that the propagation direction of the wave depends on the phase distribution of its wave front. Assume waves within two adjacent ray tubes travel across the interface in Fig. 4b. The phase matching condition on the interface leads to

$$\boldsymbol{K}_i \boldsymbol{r} = \boldsymbol{K}_r \boldsymbol{r} = \boldsymbol{K}_t \boldsymbol{r}, \tag{15}$$

where $\boldsymbol{K}_i$, $\boldsymbol{K}_r$, and $\boldsymbol{K}_t$ are wave vectors of incidence, reflection, and refraction, respectively, and $\boldsymbol{r}$ is the position vector of any point on the interface.
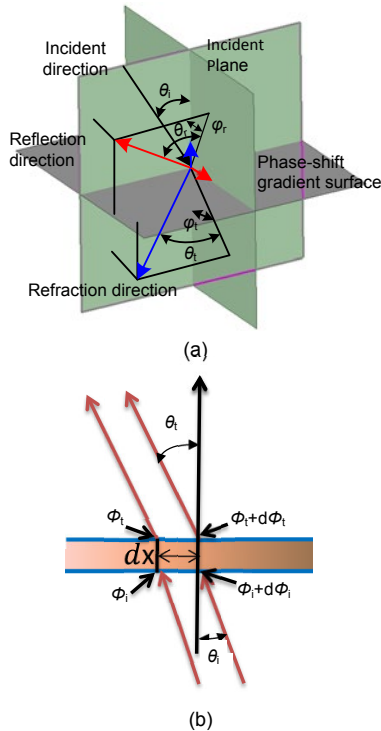

(a)

(b)

Fig. 4 Schematic used to derive the 2D generalized Snell law (a) and to show the principles of the generalized laws of refraction (b)
(a) is reprinted from Yu et al. (2013), Copyright 2013, with permission from IEEE. (b) is reprinted from Zhang PF et al. (2017), Copyright 2017, with permission from IEEE

Eq. (15) can be written in its component form as

$$\begin{cases} K_{ix}\mathrm{d}x + K_{iy}\mathrm{d}y = K_{rx}\mathrm{d}x + K_{ry}\mathrm{d}y, \\ K_{ix}\mathrm{d}x + K_{iy}\mathrm{d}y = K_{tx}\mathrm{d}x + K_{ty}\mathrm{d}y. \end{cases} \tag{16}$$

Eq. (16) represents the basis of the classical Snell law governing the reflection and refraction of the wave, which can be expressed as

$$\begin{cases} \text{For reflection}: \begin{cases} \theta_r = \theta_i, \\ \varphi_r = \varphi_i, \end{cases} \\ \text{For refraction}: \begin{cases} \dfrac{\sin\theta_i}{\sin\theta_t} = \dfrac{n_t}{n_i}, \\ \varphi_t = \varphi_i. \end{cases} \end{cases} \tag{17}$$

Now, if we insert a surface which supports a non-uniform phase shift $\Phi_r^\delta(x, y)$ at the interface, the phase matching condition can be rewritten as

$$\begin{cases} \text{For reflection}: K_{ix}x + K_{iy}y + \Phi_r^\delta(x,y) = K_{rx}x + K_{ry}y, \\ \text{For refraction}: K_{ix}x + K_{iy}y + \Phi_t^\delta(x,y) = K_{tx}x + K_{ty}y. \end{cases} \tag{18}$$

From Eq. (18) we can derive the conventional generalized Snell law as

$$\begin{cases} \text{For reflection}: \begin{cases} K_{ix} + \dfrac{\partial \Phi_r}{\partial x} = K_{rx}, \\ K_{iy} + \dfrac{\partial \Phi_r}{\partial y} = K_{ry}, \end{cases} \\ \text{For refraction}: \begin{cases} K_{ix} + \dfrac{\partial \Phi_t}{\partial x} = K_{tx}, \\ K_{iy} + \dfrac{\partial \Phi_t}{\partial y} = K_{ty}. \end{cases} \end{cases} \tag{19}$$

Next, we proceed to generalize Eq. (19). We denote the indices of the material on the interface by n_i and n_t, and $\hat{n}$ or $\hat{z}$ as the normal direction of the interface. Since $\Phi_{t/r}^\delta(x, y)$ is defined on the interface, we can set $\dfrac{\partial \Phi_{t/r}^\delta}{\partial z} = 0$ and extend the gradient of $\Phi_{t/r}^\delta$

as $\quad \nabla \Phi_{r/t}^\delta = \dfrac{\partial \Phi_{r/t}}{\partial x}\hat{x} + \dfrac{\partial \Phi_{r/t}}{\partial y}\hat{y} + \dfrac{\partial \Phi_{r/t}}{\partial z}\hat{z}.$ Taking a

relationship into consideration, which is expressed as

$$
\begin{cases}
K_{\mathrm{t}z} = K_{\mathrm{i}z} - 2K_0 n_{\mathrm{i}} \left(\hat{k}_{\mathrm{i}} \cdot \hat{z} \right), \\
K_{\mathrm{t}z} = K_{\mathrm{i}z} - K_0 \left[n_{\mathrm{i}} \left(\hat{k}_{\mathrm{i}} \cdot \hat{z} \right) + \sqrt{n_{\mathrm{t}}^2 - \left(n_{\mathrm{i}} \left| \hat{k}_{\mathrm{i}} \times \hat{z} \right| \right)^2} \right],
\end{cases}
\tag{20}
$$

we obtain a more concise formula of the generalized Snell law, which is independent of the local 2D coordinate limitation, expressed as

$$
\begin{cases}
\boldsymbol{K}_{\mathrm{r}} = \boldsymbol{K}_{\mathrm{i}} - 2K_0 n_{\mathrm{i}} \hat{n} \left(\hat{k}_{\mathrm{i}} \cdot \hat{n} \right), \\
\boldsymbol{K}_{\mathrm{t}} = \boldsymbol{K}_{\mathrm{i}} - \hat{n} K_0 \left[n_{\mathrm{i}} \left(\hat{k}_{\mathrm{i}} \cdot \hat{n} \right) + \sqrt{n_{\mathrm{t}}^2 - \left(n_{\mathrm{i}} \left| \hat{k}_{\mathrm{i}} \times \hat{n} \right| \right)^2} \right].
\end{cases}
\tag{21}
$$

Now, we explore whether we can break the limitations of the conventional reflection and refraction processes set by the critical angle.

It is well known that in traditional refraction, when the incident angle is larger than the critical angle $\theta_{\mathrm{c,i}} = \arcsin(n_{\mathrm{t}}/n_{\mathrm{i}})$, the refraction angle will be beyond 90°. In this case, the total refraction will occur, and no energy would be transmitted through the interface. However, if the surface has a non-uniform phase shift $\varPhi_{\mathrm{t}}^{\delta}$, we earn a new freedom to control the critical angle by $\varPhi_{\mathrm{t}}^{\delta}$. This is because according to Eq. (19), the refraction angle can be written as Eq. (22) (see the bottom of this page).

Hence, when the refraction angle equals 90°, the critical angle satisfies Eq. (23) (see the bottom of this page).

Eqs. (22) and (23) enable us to determine whether there will be a total refraction, since this

phenomenon is determined by not only incident angle θ_{i} but also φ_{i}, $\varPhi_{\mathrm{t}}^{\delta}$, and n_{t}.

For the simplified 2D case, for which $\partial \varPhi_{\mathrm{t}}^{\delta}/\partial y = 0$, the critical angle can be written as

$$
\theta_{\mathrm{c,i}}' = \arcsin \left[\frac{1}{n_{\mathrm{i}}} \left(n_{\mathrm{t}} - \frac{1}{k_0} \frac{\partial \varPhi_{\mathrm{t}}^{\delta}}{\partial x} \right) \right],
\tag{24}
$$

which implies, in turn, that if the phase shift gradient $\partial \varPhi / \partial x$ is negative, it would result in a critical angle larger than $\theta_{\mathrm{c,i}} = \arcsin(n_{\mathrm{t}}/n_{\mathrm{i}})$.

Another interesting attribute of the GSL is that there exists a critical angle of reflection which is not the case in the conventional Snell law, in which the reflected angle is always equal to the incident angle. However, for the present case, we can find the generalized reflection angle expressed as Eq. (25) (see the top of the next page).

Eq. (25) shows that there exists a critical angle for reflection that satisfies the condition given in Eq. (26) (see the top of the next page).

For the simplified 2D case mentioned above, the critical reflection angle is written as

$$
\theta_{\mathrm{i}} = \arcsin \left(1 - \frac{1}{n_{\mathrm{i}}} \frac{1}{k_0} \frac{\partial \varPhi_{\mathrm{r}}^{\delta}}{\partial x} \right).
\tag{27}
$$

Eq. (27) shows that if the phase shift gradient $\partial \varPhi_{\mathrm{r}}^{\delta} / \partial x$ is negative, the reflection angle will reach 90° before the incident angle reaches grazing incidence, i.e., 90°. In contrast, if the phase shift gradient $\partial \varPhi_{\mathrm{r}}^{\delta} / \partial x$ is positive, the grazing-incidence wave can generate a reflected wave, which deviates from the direction of grazing incidence.

$$
\begin{cases}
\varphi_{\mathrm{t}} = \arctan \left(\dfrac{n_{\mathrm{i}} \sin \theta_{\mathrm{i}} \sin \varphi_{\mathrm{i}} + \dfrac{1}{k_0} \dfrac{\partial \varPhi_{\mathrm{t}}^{\delta}}{\partial y}}{n_{\mathrm{i}} \sin \theta_{\mathrm{i}} \cos \varphi_{\mathrm{i}} + \dfrac{1}{k_0} \dfrac{\partial \varPhi_{\mathrm{t}}^{\delta}}{\partial x}} \right), \\[4mm]
\theta_{\mathrm{t}} = \arcsin \left\{ \dfrac{1}{n_{\mathrm{t}}} \left[\left(n_{\mathrm{i}} \sin \theta_{\mathrm{i}} \cos \varphi_{\mathrm{i}} + \dfrac{1}{k_0} \dfrac{\partial \varPhi_{\mathrm{t}}^{\delta}}{\partial x} \right)^2 + \left(n_{\mathrm{i}} \sin \theta_{\mathrm{i}} \sin \varphi_{\mathrm{i}} + \dfrac{1}{k_0} \dfrac{\partial \varPhi_{\mathrm{t}}^{\delta}}{\partial y} \right)^2 \right]^{\frac{1}{2}} \right\}.
\end{cases}
\tag{22}
$$

$$
\left[\left(n_{\mathrm{i}} \sin \theta_{\mathrm{c,i}}' \cos \varphi_{\mathrm{i}} + \frac{1}{k_0} \frac{\partial \varPhi_{\mathrm{t}}^{\delta}}{\partial x} \right)^2 + \left(n_{\mathrm{i}} \sin \theta_{\mathrm{c,i}}' \cos \varphi_{\mathrm{i}} + \frac{1}{k_0} \frac{\partial \varPhi_{\mathrm{t}}^{\delta}}{\partial y} \right)^2 \right]^{\frac{1}{2}} = n_{\mathrm{t}}.
\tag{23}
$$

$$\begin{cases} \varphi_r = \arctan\left(\dfrac{n_i \sin\theta_i \sin\varphi_i + \dfrac{1}{k_0}\dfrac{\partial \Phi_r^\delta}{\partial y}}{n_i \sin\theta_i \cos\varphi_i + \dfrac{1}{k_0}\dfrac{\partial \Phi_r^\delta}{\partial x}} \right), \\[4mm] \theta_r = \arcsin\left[\left(\sin\theta_i \cos\varphi_i + \dfrac{1}{n_i}\dfrac{1}{k_0}\dfrac{\partial \Phi_r^\delta}{\partial x} \right)^2 + \left(\sin\theta_i \sin\varphi_i + \dfrac{1}{n_i}\dfrac{1}{k_0}\dfrac{\partial \Phi_r^\delta}{\partial y} \right)^2 \right]^{\frac{1}{2}}. \end{cases} \tag{25}$$

$$\left[\left(\sin\theta_i \cos\varphi_i + \frac{1}{n_i}\frac{1}{k_0}\frac{\partial \Phi_r^\delta}{\partial x} \right)^2 + \left(\sin\theta_i \sin\varphi_i + \frac{1}{n_i}\frac{1}{k_0}\frac{\partial \Phi_r^\delta}{\partial y} \right)^2 \right]^{\frac{1}{2}} = 1. \tag{26}$$

From the analysis presented above, we can see that GSL offers us the possibility of overcoming the limitations of the critical angle of conventional reflection and refraction by controlling the phase shift gradient on the interface.

We now proceed to present several examples which illustrate applications of the GSL.

Case 1: high-gain flat lens antenna

For the typical flat lens, as shown in Fig. 5, a phase shifting surface (PSS) is used to transform a spherical wave front into a planar one by modifying all the refraction angles to zero.
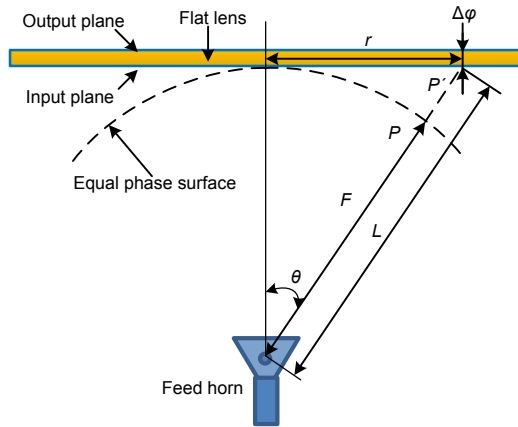

Fig. 5 Flat lens antenna with high gain

From Eq. (19), one can find the relationship expressed as

$$\sin\theta_t - \sin\theta_i = k_0^{-1}\frac{d\Phi}{dx}. \tag{28}$$

Hence, equating $\theta_t=0$ leads to $d\Phi=-k_0\sin\theta_i dx$. Let the phase delay at the center of the lens be Φ_0. The phase delay at point x_p is the sum of Φ_0 and the integral of the phase gradient, expressed as

$$\Phi(x_p) = \Phi_0 + \int_0^{x_p} (-k_0\sin\theta_i)dx. \tag{29}$$

Point x_p is located at a distance of x_r from the center. Based on $\theta_i=\arctan(x/F)$ and $dx=F(\cos\theta_i)^{-2}d\theta_i$, Eq. (29) can be rewritten as

$$\begin{aligned} \Phi(\theta) &= \Phi_0 + \int_0^{x_p} \left[-k_0 F\sin\theta_i(\cos\theta_i)^{-2} \right]d\theta_i \\ &= \Phi_0 + F[1-(\cos\theta)^{-1}], \end{aligned} \tag{30}$$

where F is the focal length.

It is evident that the phase shift of $F[1-(\cos\theta)^{-1}]+\Phi_0$ can compensate for the phase delay introduced by the path difference. This is consistent with the results of the conventional geometrical optical approach. Thus, GSL provides another way to look at the problem of designing a flat lens.

Case 2: phased array

Traditional phased arrays (Fig. 6) control the beam steering direction by phase shifting the radiation fields of all elements. From the point of view of the GSL, we can take the feeding system of a phased array as a plane wave with incident angle of $\theta_i=0$. The object, then, is to modify the refraction of the wave to the desired beam steering direction, namely $\theta_t=\theta_d$. Hence, if the phase difference and distance between two adjacent cells are designated as $d\Phi$ and dx, respectively, then by substituting $\theta_i=0$ into Eq. (28), we can obtain Eq. (31), which is exactly the same as the conventional relationship used to design a phased array:

$$\theta_{\mathrm{t}} = \arcsin\left(\frac{1}{k_0}\frac{\mathrm{d}\varPhi}{\mathrm{d}x}\right). \tag{31}$$

Case 3: reflect array

Consider an example for the reflected phase shift from the reflect array surface using the GSL (Fig. 7). We can obtain

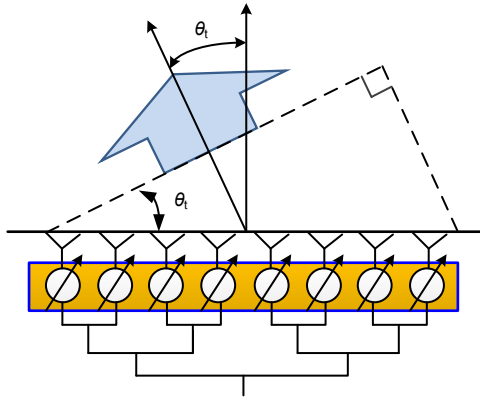$$\varPhi(\theta) - \varPhi(0) = k_0 H - k_0 \frac{H}{\cos\theta}. \tag{32}$$

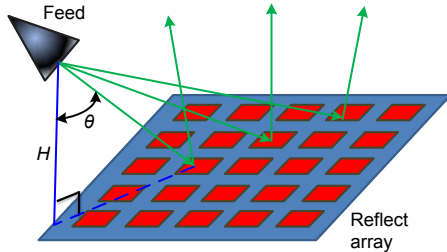**Fig. 6 Schematic used to show the principles of the phased array**

Fig. 7 Schematic used to show the principles of the reflect array
Reprinted from Zhang PF et al. (2017), Copyright 2017, with permission from IEEE

Case 4: beam shaping

The GSL not only provides an alternative way to look at some familiar antenna design problems mentioned above, but also offers a new way to realize more complex manipulations of the field with a view to enhance the performance of an antenna.

As an example, GSL can be used to generate orbital angular momentum (OAM) (Fig. 8).

Another application of the GSL is translating the capability of field manipulation into beam
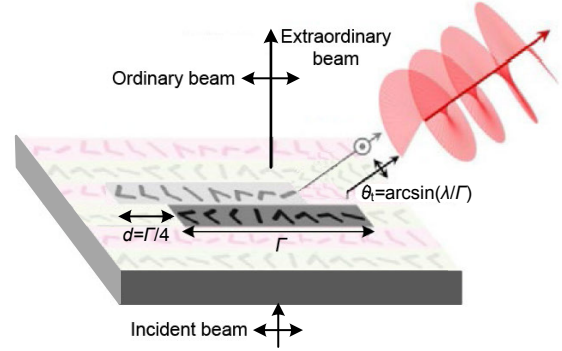
Fig. 8 Schematic showing the working mechanism of a metasurface to generate orbital angular momentum
Reprinted from Yu et al. (2013), Copyright 2013, with permission from IEEE

manipulation. As shown in Zhang PF et al. (2017), a flat metasurface lens can be designed based on GSL to reshape the beam of the feed horn into a desired one. The beam impinging upon the input port of the lens is regarded as a set of ray tubes (Fig. 9). The lens, which is composed of PSSs, modifies the direction of each ray tube using the surface with phase shift gradients to generate the desired beam, such as a flat top or an ISO_flux beam.

This method has been further extended to design a conformal lens with the capability of beam shaping (Zhang PF et al., 2018). Such a design has the advantage that it can be embedded within a conformal radome, which is desirable.

Readers can refer to Achouri et al. (2015) and Jia et al. (2018) for further exploration, where the generalized sheet transition conditions have been presented and used to generate two independent beams based on a metasurface (Fig. 9d).

The above examples verify that the GSL can be used to generate desired overall effect by manipulating the local refraction.

4.2 Further discussion on surface electromagnetic

While SEM uses the GSL, which manipulates the field based on phase gradient, the SEM is not limited just to the use of GSL. We now mention some other EM field manipulation methods based on the use of a metasurface, which have been proposed by Cui et al. (2014).

Case 1: coding metasurface

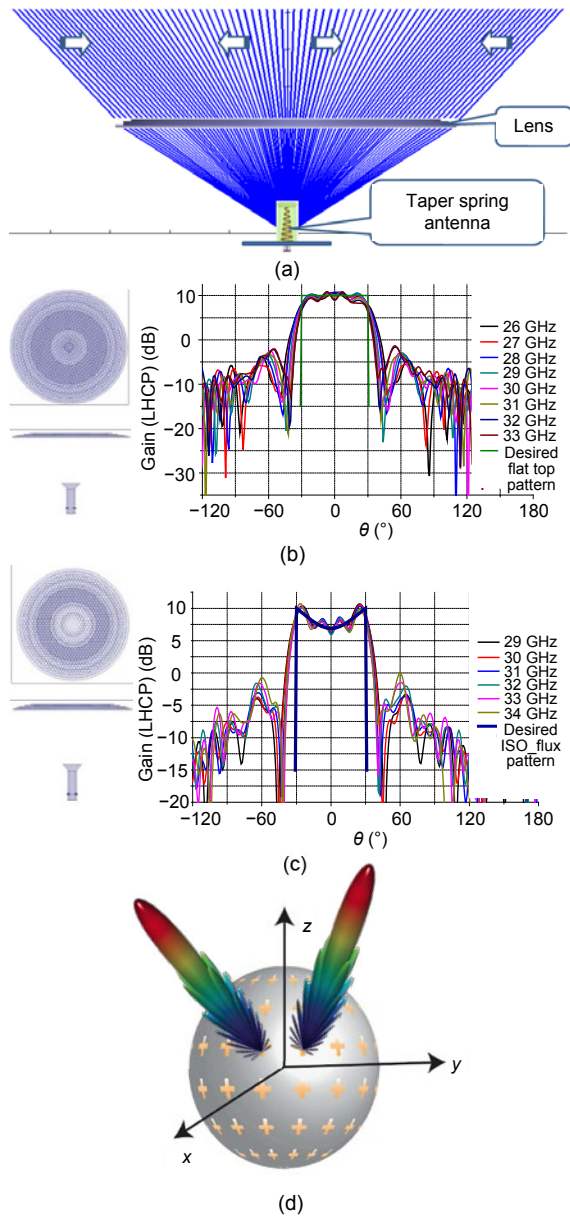Coding metasurfaces are known as digital metasurfaces and programmable metasurfaces. A

Fig. 9 Beam shaping based on GSL: (a) ray trace; (b) lens and flat top beam; (c) lens and ISO_flux beam; (d) metasurface generating a simultaneous multi-beam
(a)–(c) are reprinted from Zhang PF et al. (2017), Copyright 2017, with permission from IEEE. (d) is derived from a presentation and published with authorization from the authors

typical design of the programmable metasurface includes several steps. We first design a cell (Fig. 10), and it includes state controllers, such as biased diodes which can switch between different working states according to the status of controllers. The cells can provide different responses, such as 0, $\pi/2$, π, and $3\pi/2$ phase responses, which are referred to as 00, 01, 10,

and 11 states, respectively. Then, a field programmable gate array (FPGA) is used to trigger the controllers, which serve to control the working states of each cell. Finally, dedicated codes are developed to sequentially control the working states of all cells to achieve the desired goal, which may generate the desired field manipulation results, such as radar cross section (RCS) reduction (Fig. 11).
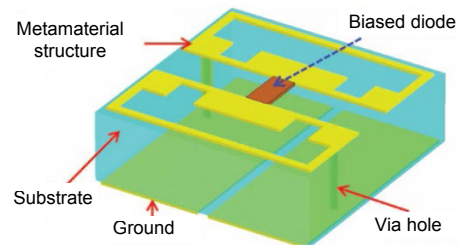

Fig. 10 Cell of coding metasurface
Reprinted from Cui et al. (2014), Copyright 2014, with permission from Springer Nature, licensed under CC BY 4.0

The programmable metasurface modifies the synchronous response of all cells not only depending on their spatial positions, but also in time sequence. Results show that both the spatial and frequency spectra are modified or manipulated by the metasurface in a programmable way. This, in turn, has the potential of controlling the radiation patterns of antennas, thus reducing the RCS of radar targets and realizing smart metamaterials.

An application of the fast real-time digital programmable metasurface has been reported (Li et al., 2019), which presents a real-time digital-metasurface imager (Fig. 12). A programmable metasurface is trained in situ to generate the radiation patterns using machine learning of optimized measurement modes. The metasurface, antenna, or imager is electronically reprogrammed in real time to access the optimized solution for an entire data set, thus realizing storage and transfer of full-resolution raw data in dynamically varying scenes (Li et al., 2019). The new imaging system overcomes the problems of time-consuming data acquisition and complex reconstruction algorithms for post-processing of data, in a way different from that used by conventional radar.

Case 2: Fabry-Perot cavity antennas based on partially reflecting surfaces
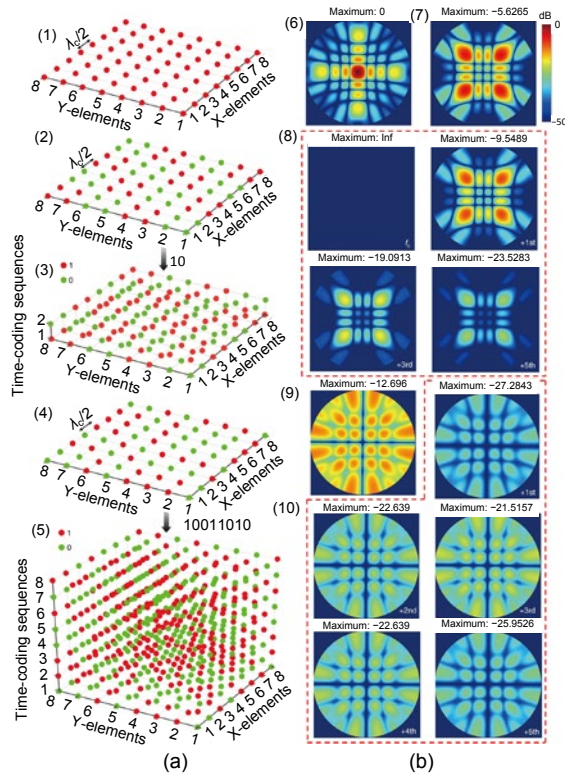
Fig. 11 Radar cross section (RCS) reductions via space-time-coding metasurfaces: (a) development of space-time-coding; (b) scattering patterns at different harmonic frequencies pertaining to different space-time-coding strategies

Reprinted from Zhang L et al. (2018), Copyright 2018, with permission from Springer Nature, licensed under CC BY 4.0
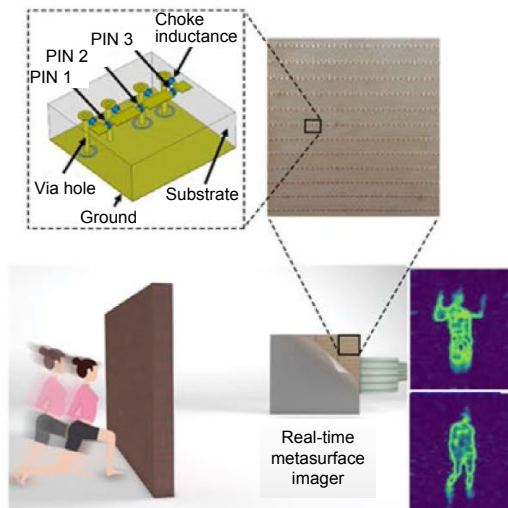

Fig. 12 Illustration of a real-time reprogrammable metasurface imager imaging a moving person behind a wall

Reprinted from Li et al. (2019), Copyright 2019, with permission from Springer Nature, licensed under CC BY 4.0

As shown in Fig. 13, a Fabry-Perot cavity antenna (FPCA) generally consists of an antenna feed, a metal ground plane, and a partially reflecting surface (PRS) to form a resonator (Wei et al., 2016). When the space between these two plates is approximately half a wavelength, the forward radiation impinging on the PRS can be enhanced using in-phase multiple bounces of the field within FPCA. We can see that the FPCA provides another example of manipulating the field by controlling the reflection together with the phase delay during multiple bounces. It can generate a high-gain beam just using a single-feed system with low complexity (Liu ZG, 2010).
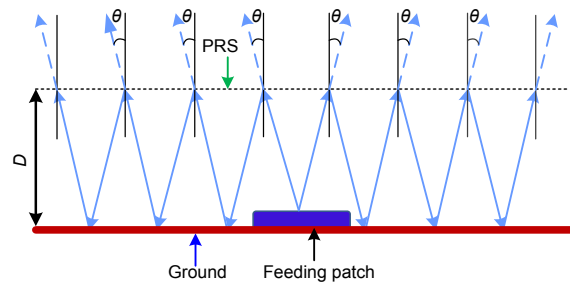

Fig. 13 Model of the Fabry-Perot cavity antenna with partially reflecting surfaces (PRS)

For flexible control of the FPCA to improve its performance, various methods based on magnitude manipulation, phase manipulation, or both of EM fields have been introduced (Fig. 14). Design of the top cover of the FPCA takes cues from the design of PRS (made by wires or strips), single-layered dense dielectric sheet (Marin et al., 2019), multilayered dielectric sheet, electronic band gap (EBG) materials, frequency selective surface (FSS) (Lee C et al., 2018), and metamaterials. The ground plane can be modified by replacing it by high-impedance surface (HIS) with zero phase delay to decrease the thickness of the antenna (Lee JG and Lee, 2017), using a polarization transformation surface to manipulate the polarization, or using curved ground to modify the aperture distribution (Liu ZG, 2016). The feed is modified for multi-feed configuration (Wei et al., 2016) and reconfigurable and dual polarization design (Lian et al., 2017).

These modifications can enhance the performance of the FPCA and provide it the capability of beam steering (Ratni et al., 2018) or scanning, low profile, and polarization control.
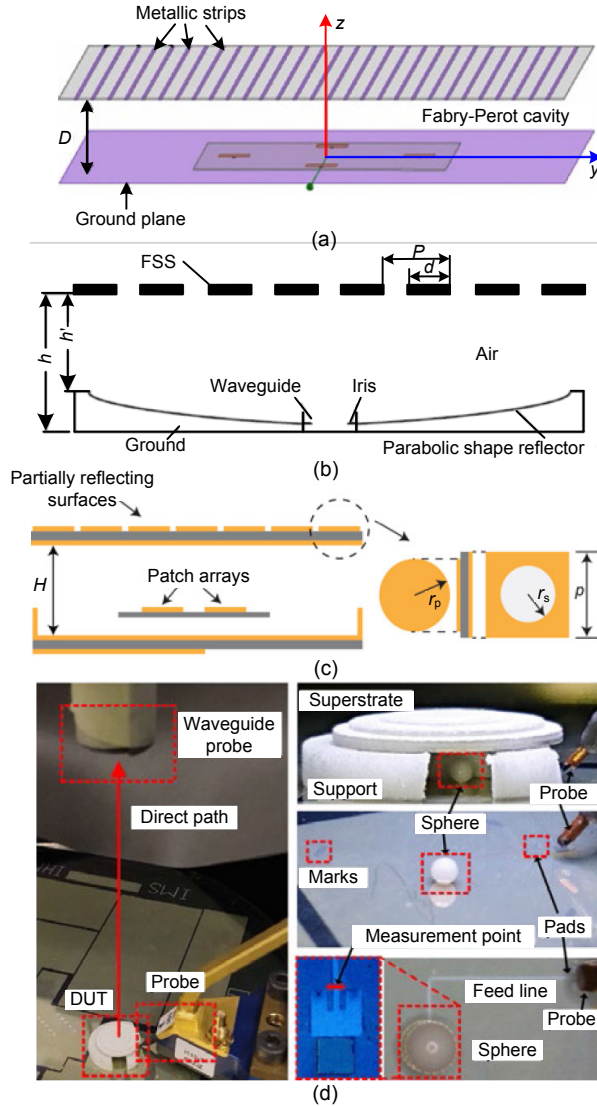
Fig. 14   Multi-feed Fabry-Perot cavity antenna (FPCA) (a), broadband FPCA with a parabolic shape reflector (b), reconfigurable FPCA (Lian et al., 2017) (c), and FPCA with multilayered dielectric sheets (Marin et al., 2019) (d)
(a) is reprinted from Wei et al. (2016), Copyright 2016, with permission from IEEE. (b) is reprinted from Liu ZG (2016), Copyright 2016, with permission from IEEE

5   Performing a mathematical operation with field manipulation

A new concept of computational metamaterials (CMs) has been introduced (Silva et al., 2014), where metamaterials serve as analog computers to perform mathematical operations, such as spatial differentiation, integration, and convolution. The CMs have the potential of providing the possibility of realizing a highly compact and potentially integrable analog computer, offering a new approach to field manipulation.

Fig. 15 shows the conceptual sketch of mathematical computing based on field manipulation of a metasurface. The system consists of three cascaded sub-blocks: a Fourier transform sub-block, a suitably tailored matasurface (MS) spatial filter, and an inverse Fourier transform sub-block.

The first-order derivative of $g(y) \rightarrow \mathrm{d}f(y)/\mathrm{d}y$ is considered for simplification. The strategy is to transform the derivative operation of $\mathrm{d}f(y)/\mathrm{d}y$ into the products of $\tilde{f}(k_y)$ and $\mathrm{i}k_y$, where $\tilde{f}(k_y)$ is the Fourier transform of $f(y)$. Here, the traditional graded-index (GRIN) dielectric slab with permeability $\mu = \mu_0$ and parabolic variation of permittivity $\varepsilon(y) = \varepsilon_c \{1 - [\pi/(2L_g)]^2 y^2\}$ forms the first sub-block. It is marked as GRIN(+) and used to transfer $f(y)$ to its Fourier transform $\tilde{f}(k_y)$. A suitably tailored MS spatial filter for the Green function $\mathrm{i}k_y$ is realized by thin MS with relevant parameters and permeability to achieve the normalized transfer function proportional to $\mathrm{i}y(W/2)$. The required parameters and permeability are given by

$$\frac{\varepsilon_{ms}(y)}{\varepsilon_0} = \frac{\mu_{ms}(y)}{\mu_0} = \mathrm{i}\frac{\lambda_0}{2\pi\Delta}\ln\left(\frac{-\mathrm{i}W}{2y}\right). \qquad (33)$$

For the inverse Fourier transform, i.e., sub-block GRIN(−), an ideal GRIN structure is used with negative parameters of permeability $\mu = -\mu_0$ and permittivity $\varepsilon = -\varepsilon(y)$ to transfer the results from $\tilde{f}(k_y) \cdot \mathrm{i}k_y$ to $g(y) \rightarrow \mathrm{d}f(y)/\mathrm{d}y$.

Simulation results have shown that CMs do manipulate the field to realize the mathematical operation.

This example provides another model for combining 3D field manipulation within GRIN and 2D manipulation using a metasurface. If the performance of the mathematical operation can be integrated into the antenna system within the framework of field manipulation, the antenna may play a more powerful role in the future.
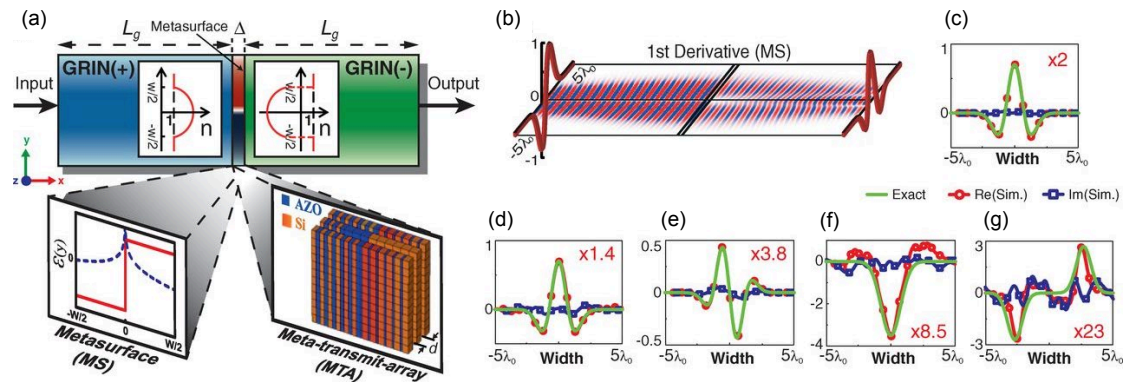
Fig. 15 Metamaterial computing using metasurfaces: (a) illustration of metamaterial computing using metasurfaces; (b) perspective views of the input and output functions; (c) simulation results of metamaterial computing using metamaterial for the first differentiation of the input function; (d) simulation results of metamaterial computing using meta-transmit-array for the first differentiation of the input function; (e) simulation results of metamaterial computing using metamaterial for the second differentiation of input function; (f) simulation results of the second differentiation operation; (g) simulation results of the convolution operation
Reprinted from Silva et al. (2014), Copyright 2014, with permission from AAAS

6 Conclusions

In this work, we have presented two different field manipulation techniques, i.e., 3D transformation electromagnetics and 2D surface electromagnetics, and their applications in antenna design. Our primary motivation has been to see if we could develop a robust and general-purpose tool for innovative design of antennas for future communication. The 3D field manipulation technique has been originally developed for such as cloaking application; however, it has been adopted here for antenna design, as it has the 2D surface electromagnetics approach. Some important issues, such as imposition of boundary conditions on the interface between the transformed medium and free space, require close attention during the design process of cloaks and have been identified. Finally, some new concepts of antennas designed for wireless communication and imaging, such as real-time programmable metasurface imaging antennas and beam formers, have been introduced.

Before closing this paper, we take the liberty to speculate on the directions of field manipulation for designing antennas in the future. First, we hasten to point out that our primary emphasis has been to lay the foundations of the theoretical aspects of various field manipulation techniques. Although we have mentioned a variety of applications of the field manipulation techniques in this study, most of the designs presented herein have not been realized for real-world applications because of the lack of available materials dictated by the field manipulation techniques. The required materials should have low loss and wideband, and have low dispersion attributes that are highly desirable for most practical antenna applications. Nonetheless, we set the stage for further exploration and practical realization of the materials which are needed to fabricate the desired devices (antennas). It is our sincere hope that researchers in the area will vigorously pursue this aspect of the research, and help bridge the gap that exists today between the theory and practice of the field manipulation techniques, either for designing real-word antennas for novel applications in the future, or for realizing improvements of the performance of existing antennas, to give performance that is not possible hitherto using conventional antenna design techniques.

Contributors

Peng-fei ZHANG, Yu-kai YAN, and Raj MITTRA drafted the manuscript. Peng-fei ZHANG derived the formulas presented in Section 4.1. Ying LIU and Raj MITTRA revised and finalized the paper.

Compliance with ethics guidelines

Peng-fei ZHANG, Yu-kai YAN, Ying LIU, and Raj MITTRA declare that they have no conflict of interest.

References

Achouri K, Salem MA, Caloz C, 2015. General metasurface synthesis based on susceptibility tensors. *IEEE Trans Antenn Propag*, 63(7):2977-2991.
https://doi.org/10.1109/TAP.2015.2423700

Cui TJ, Qi MQ, Wan X, et al., 2014. Coding metamaterials, digital metamaterials and programmable metamaterials. *Light Sci Appl*, 3(10):e218.
https://doi.org/10.1038/lsa.2014.99

Jia X, Yang F, Vahabzadeh Y, et al., 2018. Multiple beam forming using spherical metasurfaces. IEEE Int Symp on Antennas and Propagation & USNC/URSI National Radio Science Meeting, p.1709-1710.
https://doi.org/10.1109/APUSNCURSINRSM.2018.8608223

Jiang WX, Chin JY, Li Z, et al., 2008. Analytical design of conformally invisible cloaks for arbitrarily shaped objects. *Phys Rev E*, 77(6):066607.
https://doi.org/10.1103/PhysRevE.77.066607

Kwon DH, Werner DH, 2008. Restoration of antenna parameters in scattering environments using electromagnetic cloaking. *Appl Phys Lett*, 92(11):113507.
https://doi.org/10.1063/1.2898220

Lai Y, Chen HY, Zhang ZQ, et al., 2009. Complementary media invisibility cloak that cloaks objects at a distance outside the cloaking shell. *Phys Rev Lett*, 102(9):093901.
https://doi.org/10.1103/PhysRevLett.102.093901

Lee C, Sainati R, Franklin RR, 2018. Frequency selective surface effects on a coplanar waveguide feedline in Fabry-Perot cavity antenna systems. *IEEE Antenn Wirel Propag Lett*, 17(5):768-771.
https://doi.org/10.1109/LAWP.2018.2815343

Lee JG, Lee JH, 2017. Low-profile Fabry-Perot cavity (FPC) antenna using meta-surface for dual-band. Int Symp on Antennas and Propagation, p.1-2.
https://doi.org/10.1109/ISANP.2017.8228943

Leonhardt U, 2006. Optical conformal mapping. *Science*, 312(5781):1777-1780.
https://doi.org/10.1126/science.1126493

Li LL, Ruan HX, Liu C, et al., 2019. Machine-learning reprogrammable metasurface imager. *Nat Commun*, 10(1):1082. https://doi.org/10.1038/s41467-019-09103-2

Lian RN, Tang ZY, Yin YZ, 2017. Design of a broadband polarization-reconfigurable Fabry-Perot resonator antenna. *IEEE Antenn Wirel Propag Lett*, 17(1):122-125.
https://doi.org/10.1109/LAWP.2017.2777502

Liu R, Ji C, Mock JJ, et al., 2009. Broadband ground-plane cloak. *Science*, 323(5912):366-369.
https://doi.org/10.1126/science.1166949

Liu ZG, 2010. Fabry-Perot resonator antenna. *J Infrar Millim Terah Wave*, 31(4):391-403.
https://doi.org/10.1007/s10762-009-9605-4

Liu ZG, 2016. Broadband Fabry-Perot cavity leaky wave antenna with parabolic-shape reflector. IEEE 5th Asia-Pacific Conf on Antennas and Propagation, p.355-356.
https://doi.org/10.1109/APCAP.2016.7843240

Marin JG, Baba AA, Cuenca DL, et al., 2019. High-gain low-profile chip-fed resonant cavity antennas for millimeter-wave bands. *IEEE Antenn Wirel Propag Lett*, 18(11):2394-2398.
https://doi.org/10.1109/LAWP.2019.2926791

Mittra R, Zhou Y, Zhang P, 2016. A look at electromagnetic field transformation using transformation optics (TO): wave equation and scattering matrix formalisms. *Forum Electromagn Res Meth Appl Technol*, 15:004.

Pendry JB, Schurig D, Smith DR, 2006. Controlling electromagnetic fields. *Science*, 312(5781):1780-1782.
https://doi.org/10.1126/science.1125907

Ratni B, de Lustrac A, Piau GP, et al., 2018. Phase modulation in partially reflective surfaces for beam steering in Fabry-Perot cavity antennas. Asia-Pacific Microwave Conf, p.1052-1054.
https://doi.org/10.23919/APMC.2018.8617348

Schurig D, Pendry JB, Smith DR, 2006. Calculation of material properties and ray tracing in transformation media. *Opt Expr*, 14(21):9794-9804.
https://doi.org/10.1364/OE.14.009794

Silva A, Monticone F, Castaldi G, et al., 2014. Performing mathematical operations with metamaterials. *Science*, 343(6167):160-163.
https://doi.org/10.1126/science.1242818

Wei WL, Mahdjoubi K, Brousseau C, et al., 2016. Enhancement of directivity of an OAM antenna by using Fabry-Perot cavity. 10th European Conf on Antennas and Propagation, p.1-4.
https://doi.org/10.1109/EuCAP.2016.7481906

Yang F, Rahmat-Samii Y, 2019. Surface Electromagnetics: with Applications in Antenna, Microwave, and Optical Engineering. Cambridge University Press, Cambridge, UK.

Yang R, Tang WX, Hao Y, et al., 2011. A coordinate transformation-based broadband flat lens via microstrip array. *IEEE Antenn Wirel Propag Lett*, 10:99-102.
https://doi.org/10.1109/LAWP.2011.2112328

Yu NF, Genevet P, Kats MA, et al., 2011. Light propagation with phase discontinuities: generalized laws of reflection and refraction. *Science*, 334(6054):333-337.
https://doi.org/10.1126/science.1210713

Yu NF, Genevet P, Aieta F, et al., 2013. Flat optics: controlling wavefronts with optical antenna metasurfaces. *IEEE J Sel Top Quant Electron*, 19(3):4700423.
https://doi.org/10.1109/JSTQE.2013.2241399

Zhang L, Chen XQ, Liu S, et al., 2018. Space-time-coding digital metasurfaces. *Nat Commun*, 9(1):4334.

https://doi.org/10.1038/s41467-018-06802-0

Zhang PF, Gong SX, Mittra R, 2017. Beam-shaping technique based on generalized laws of refraction and reflection. *IEEE Trans Antenn Propag*, 66(2):771-779. https://doi.org/10.1109/TAP.2017.2778042

Zhang PF, Li P, Mittra R, 2018. On the design of conformal radomes for beam-shaping of antennas. IEEE Int Symp on Antennas and Propagation & USNC/URSI National Radio Science Meeting, p.1541-1542. https://doi.org/10.1109/APUSNCURSINRSM.2018.8608927

Zhang PF, Wang S, Li P, 2019. Analysis of some mathematical questions of transformation optics and its application to stealth carpet design. *J Electron Inform Technol*, 41(6): 1336-1343 (in Chinese). https://doi.org/10.11999/JEIT180247